ACS APPLIED MATERIALS & INTERFACES

www.acsami.org Research Article

Controlling MoS_2 Nanosheet Size and Network Conductivity through Alkylammonium Ion Selection

Anthony Dawson, Vincent Renard, Weimiao Wang, Tian Carey, Rebekah Wells, David Sanchez, Joseph Neilson, Jack Doran, Eoin Caffrey, Cian Gabbett, Paul Seifert, Martin Gerlei, Georg Duesberg, Mauricio Terrones, Zdenek Sofer, Kevin Synnatschke, and Jonathan N. Coleman*

Cite This: https://doi.org/10.1021/acsami.5c24890 **Read Online**

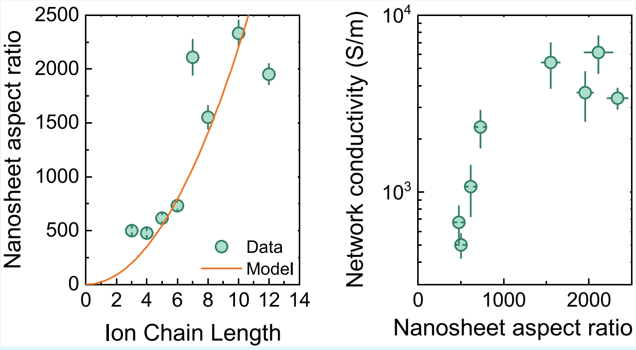

ABSTRACT: Solution-processed inks of two-dimensional (2D) semiconductors, such as molybdenum disulfide (MoS_2), hold great promise for enabling low-cost, printed electronic devices. To optimize critical performance metrics like network conductivity, large-aspect-ratio ($k_{NS} \gg 100$) nanosheets are essential to yield low-resistance flake-to-flake junctions. While electrochemical exfoliation with ammonium salts has emerged as a viable method for producing high-aspect ratio semiconducting nanosheets, the process parameters remain underexplored. In this work, we systematically investigate the role of alkylammonium ion size in the electrochemical exfoliation of MoS_2, demonstrating control over nanosheet lengths ($L \sim 1-3\ \mu m$) and nanosheet thicknesses ($t_{NS} \sim 1-4$ nm), leading to k_{NS} values between 400 and 2500. The nanosheet aspect ratio is closely linked to ion size via the energetics of exfoliation. We fabricate networks from these nanosheets and characterize their electrical properties, revealing that higher-aspect-ratio nanosheets yield significantly more conductive networks, achieving conductivities up to 6000 Sm^{1-}. Our electrical measurements show that the network conductivity is consistent with a simple model and is limited by internanosheet junctions whose resistance scales inversely with nanosheet area. These findings suggest that ion size determines nanosheet dimensions, which in turn determine network conductivity.

KEYWORDS: *solution processing, nanosheets, electrochemical exfoliation, conductivity, intercalation*

■ INTRODUCTION

Two-dimensional (2D) semiconductors have clearly demonstrated their utility as active materials for printed electronics. Networks of solution-processed semiconductors have seen applications in transistors,[1] circuits,[2] sensing,[3] photodetectors,[4] photovoltaics,[5] and thermoelectric devices.[6] Semiconducting inks of 2D nanosheets can be mass-manufactured using liquid-phase exfoliation (LPE[7]) protocols such as shear mixing. These inks can be deposited as thin films using a range of processes, including spray coating.[8] Such liquid-deposited films consist of networks of nanosheets and can have various morphologies depending on both nanosheet properties and deposition method.[9,10]

However, despite the superlative properties of individual nanosheets of 2D semiconductors, efforts to replicate these properties in networks of nanosheets have been limited by the high resistance associated with nanosheet-to-nanosheet junctions.[11] The electrical resistance across a network can be modeled as a series of nanosheet (R_{NS}) and junction (R_J) resistances, resulting in a simple model relating network conductivity to R_{NS} and R_J (see below).[11] This model shows that it is essential to achieve $R_J < R_{NS}$ to maximize network conductivity and mobility.[11−13] The electrical resistance at these junctions may be minimized by improving the alignment of nanosheets in the network and by encouraging the formation of conformal junctions between nanosheets.[9,11] Deploying techniques such as liquid−liquid interfacial self-assembly deposition has been shown to facilitate nanosheet alignment and conformality and so minimize R_J.[10,14] Recently, it was predicted that nanosheets must have aspect ratios (k_{NS}, i.e., the ratio of lateral size to thickness) above a critical value to achieve conformal and aligned junctions between the nanosheets.[12,9] Thus, to optimize the performance of printed networks, in addition to appropriate deposition methods, protocols to control the aspect ratio of the nanosheets will be required.

Received: December 12, 2025
Revised: March 24, 2026
Accepted: March 26, 2026

Electrochemical exfoliation (EE) with ammonium salts is now a well-established route for obtaining large-area (high aspect ratio) semiconducting nanosheets that retain their semiconducting phase.[15,16] EE involves driving ions between the layers of a bulk 2D crystal with a constant voltage, leading to expansion of the crystal, which facilitates subsequent exfoliation. The expanded material is then sonicated to exfoliate and disperse the material in a solvent before size selection by centrifugation. While there is now a significant amount of literature on the EE of 2D semiconductors, often focusing on a final device, relatively few studies approach the optimization of the intercalation parameter space.[13,16] Yang et al. have shown that increasing the voltage (>7 V) and sonication time (>2 h) can significantly decrease the layer number of EE silver chromium disulfide, $AgCrS_2$ nanosheets, down to a bilayer material.[17] In addition, the mechanical properties of the bulk crystals have also been shown to affect the success of the EE process. Lin et al. attribute their monolayer indium(III) selenide, In_2Se_3 nanosheets (aspect ratio ~ 300), to having a lower in-plane Young's modulus (E_{in} < 80 GPa) than other typical 2D crystals such as MoS_2, $MoSe_2$, and WSe_2 (E_{in} ≈ 200 GPa).[18] More recently, it has been found that while some materials with low in-plane Young's modulus, such as $SnSe_2$ (E_{in} = 87 GPa), exfoliate well, others with similarly low E_{in}, such as $PdSe_2$ (E_{in} = 72 GPa), do not expand well.[7] This implies that, as with liquid phase exfoliation,[19] the out-of-plane Young's modulus is also important for achieving high AR. Indeed, Carey et al. found that high values of the ratio, E_{in}/E_{out}, are critical for ensuring bulk crystal expansion during the electrochemical process and for achieving higher aspect ratio nanosheets (>1000).[13] Despite this progress, understanding the dynamic behavior of these layered materials under external stimuli remains an active area of research.[20]

The most common route to electrochemically expand MoS_2 is through the intercalation of alkylammonium salts into a host crystal. In this paper, we will discuss a number of such salts, as listed in Table 1, using an abbreviation based on the length of the salt's alkyl chain (Cn, where n is the number of carbons per chain).[14,18] Common routes include tetraheptylammonium bromide (C7),[14,18] tetrapropylammonium bromide (C3),[1,21−23] and tetrabutylammonium bromide (C4).[21] Other less common routes, including tetraethylammonium bromide (C2),[15] tetraoctylammonium bromide,[24,25] and tetradecylammonium bromide (C10),[15] have also been demonstrated. These salts were selected to form a systematic series of alkylammonium ions (C3−C12), enabling a direct investigation of how alkyl chain length affects nanosheet properties. The ions from C2 to C10 were selected based on literature precedence and commercial availability, with C12 selected to extend the series. Tetraheptylammonium bromide (C7) in the solvent acetonitrile is often preferred due to the quality of the nanosheets produced, with mean nanosheet lengths (L_{NS}) between 0.5 and 2 μm and mean nanosheet thicknesses (t_{NS}) between 2 and 5 nm,[14,15] while smaller ions like tetrapropylammonium (C3) and tetrabutylammonium bromide (C4) in the solvent propylene carbonate enable rapid expansion but typically yield lower-aspect-ratio nanosheets.[26]

We emphasize that ion selection is fundamentally linked to solvent choice. For example, polar solvents such as propylene carbonate dissolve shorter-chain ions (C3−C6) effectively, whereas larger hydrophobic ions (C7 and larger) require less polar solvents such as acetonitrile to dissolve the salt and successfully expand the crystal.[16] More complex solvent effects also exist. For example, propylene carbonate has been shown to have its own intercalation effect, enabling milder exfoliation.[21] Nevertheless, there may still be scope for optimizing solvent choice for nanosheet yields and quality.

Table 1. Quaternary Ammonium Ions[a]

full Name	abbreviation	alkyl chain length	total carbons in ion (4 × *n*)
tetraethylammonium bromide	TEAB	C2	8
tetrapropylammonium bromide	TPAB	C3	12
tetrabutylammonium bromide	TBAB	C4	16
tetrapentylammonium bromide	TPentAB	C5	20
tetrahexylammonium bromide	THxAB	C6	24
tetraheptylammonium bromide	THepAB	C7	28
tetraoctylammonium bromide	TOAB	C8	32
tetradecylammonium bromide	TDAB	C10	40
tetradodecylammonium bromide	TDoAB	C12	48

[a] A Range of Quaternary Ammonium Ions with their Respective Alkyl Chain Lengths and Total Number of Carbons, with C12 being the Largest and C2 the Smallest. Ions are denoted as "C*n*" where *n* indicates the number of carbon atoms in each alkyl chain. Each quaternary ammonium ion has four identical alkyl chains, giving a total number of carbons in each ion = (4 × *n*).

Previous studies have established that ion size influences the expansion of intercalated crystals in EE, with larger ions generally leading to greater interlayer spacing, as measured by techniques like X-ray diffraction (XRD),[15] or at a local level by scanning electron microscope (SEM).[16] However, these techniques provide an incomplete picture. XRD offers a bulk average of interlayer spacing but does not give information about the lateral size or thickness of nanosheets, and SEM analysis cannot provide good statistical data on the exfoliated product.

Critically, the field lacks a systematic and quantitative link between intercalant ion size and the statistical dimensions ($<L_{NS}>$, $< t_{NS}>$, or the mean nanosheet aspect ratio, $< k_{NS>}$) of the exfoliated nanosheets. It remains an open question whether crystal expansion directly translates to larger, thinner, and higher-quality nanosheets in solution. Furthermore, while ion size has been explored from the perspective of intercalation efficiency, its downstream effects have so far been overlooked, particularly how this ion-driven control over nanosheet dimensions dictates the electrical performance of printed networks of nanosheets.[18,27,28]

In this article, we close this knowledge gap by systematically examining the entire pathway from ion selection to the electrical properties of printed networks. We demonstrate that alkylammonium ion size is a powerful tool for precisely tuning the dimensions of solution-processed MoS_2 nanosheets. We then quantitatively link these tailored nanosheet properties to the electrical properties of the thin-film networks. This study moves beyond observation of crystal expansion and establishes a design rule for EE: ion selection enables tailoring of nanosheet dimensions for optimized electronic device performance.

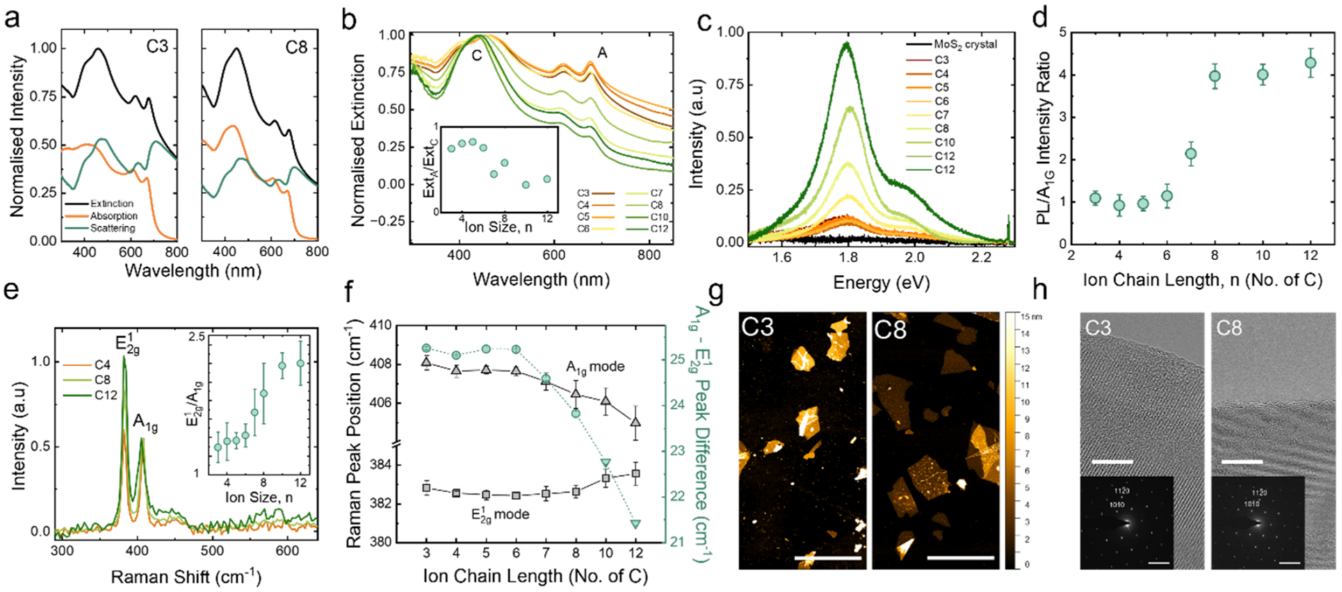

Figure 1. Nanosheet characterization. (a) UV−vis spectra of C3 and C8, respectively. (b) Overlaid extinction plots of all samples. Inset: Ratio of A-exciton peak to C-exciton peak extinction. (c) Representative PL and Raman spectra of C3−C12 inks along with the raw MoS_2 crystal. The spectra were normalized to the A_{1g} Raman mode of MoS_2 at $\sim$ 406 cm^{-1}. (d) Ratio of PL peak to Raman A_{1g} mode. (e) Raman spectra for C4, C8, and C12 ions, normalized to the A_{1g} Raman mode. Inset: Ratio of E_{2g}^{1} to A_{1g} scaling with n. (f) Positions of Raman peaks plotted with ion chain length, n. The difference in peak positions for each n is shown in green. (g) AFM images of C3 and C8 material, respectively. Each with 5 μm scale bars. (h) TEM images and inset Fourier Transforms of C3 and C8 edges, respectively. Scale bars of 10 nm in each.

RESULTS AND DISCUSSION

Material Quality

MoS_2 was electrochemically expanded by ion intercalation into bulk crystals before exfoliation (Methods). Intercalation was performed using eight different quaternary ammonium ions, C3, C4, C5, C6, C7, C8, C10, and C12 (Table 1). Preliminary experiments revealed that no single solvent system worked effectively for all ions, requiring tailored approaches for different size ranges. For the smaller ions (C3−C6), we found propylene carbonate (PC) to be a good solvent, with attempts using acetonitrile (ACN) resulting in minimal crystal expansion and poor nanosheet yield. Conversely, the midsized ions (C7 and C8) showed the opposite behavior, performing poorly in PC but achieving effective intercalation when dissolved in ACN. The largest ions (C10 and C12) presented additional challenges, requiring a modified two-step procedure: we first preintercalated the crystals using C7 in ACN to partially expand the lattice, then treated them with the target larger ion also in ACN to complete the exfoliation process.[17] To reflect the use of this preintercalation method for these two ions, these data points are depicted with different symbols in this work. C2 was also explored but did not yield stable, usable dispersions under the conditions used for other ions and was therefore excluded from the systematic study.

After intercalation, the electrolyte was drained off, and the separated intercalated material was added to a PVP-DMF solution before brief ultrasonication for 5 min to complete exfoliation. The PVP is required to facilitate stabilization of the nanosheet dispersion.[1] The exfoliated material was then centrifuged at low speed, removing bulk material, and then solvent cleaning steps were carried out to remove DMF, PVP, and any nanodots. The final material was resuspended in IPA. These inks are colloidally stable in IPA, typically for up to 2 weeks, and stable in DMF for up to one month. No significant changes in nanosheet dimensions were observed in this period. It should be noted that the electrical properties of networks made from aged (>2 weeks) inks will not be comparable to those made from fresh inks, while optical properties can degrade even faster than this, depending on storage.[29] Therefore, all samples are measured as quickly as possible and at the same stage of aging.

Figure 1a shows the UV−visible optical absorption spectra of C3 and C8 inks, obtained using an integrating sphere to separate the extinction and absorption of the inks, from which scattering can then be isolated.[30] Complete spectra for all samples can be seen in Figure S1. For all spectra, the expected strong excitonic transitions at 679 nm (A-exciton), 623 nm (B-exciton), and 440−460 nm (C-exciton) are seen. A drop in the intensity of the A excitonic peak relative to the C excitonic peak (at approximately 450 nm) in the extinction spectrum is an indicator of reduced thickness of the nanomaterial.[31,32] Figure 1b depicts the extinction spectra for each sample with the intensity ratio of the A/C excitonic peaks shown in the inset. The A/C-exciton ratio is greatest for the smaller ion chain samples (C3−C6) but decreases for the C7 to C12 inks. It is known that small A/C ratios are consistent with thinner nanosheets,[19] indicating that larger ions yield thinner flakes. The underlying cause of this behavior is that thinning the nanosheet increases quantum confinement and reduces dielectric screening. Then the higher-energy C-exciton (derived from deeper valence bands) is suppressed more strongly than the A-exciton, causing the A/C intensity ratio to decrease in the thinner layers. Figure 1c depicts the representative PL/Raman spectra of C3−C12 inks, and a clearly higher PL/Raman intensity ratio can be observed for the larger intercalating ions, suggesting a higher monolayer content in C8−C12 inks.[33,34] This is also supported by the averaged PL/E_{2g}^{1} intensity ratio in Figure 1d, where the value of C8−C12 is 3−4 times that of C3−C6. The raw crystal exhibits no appreciable photoluminescence, as expected. Taken

https://doi.org/10.1021/acsami.5c24890
ACS Appl. Mater. Interfaces XXXX, XXX, XXX−XXX

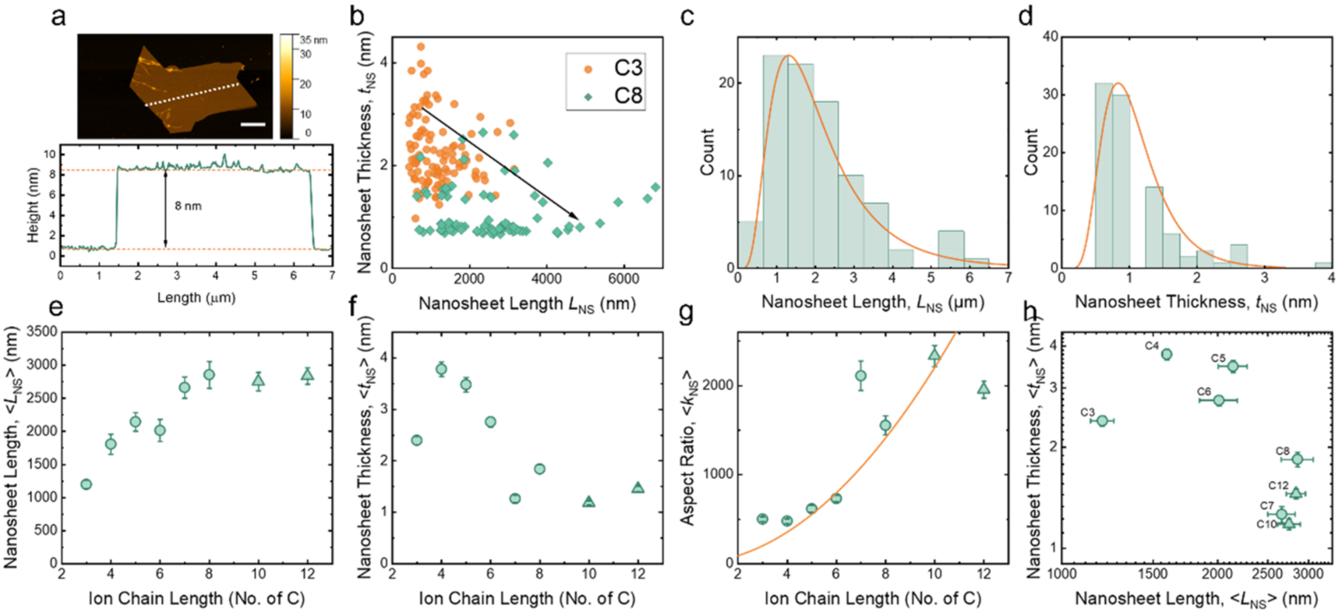

Figure 2. Size characteristics of exfoliated samples. (a) Top: AFM image of the nanosheet exfoliated using C10 with a 10 μm scale bar. Bottom: Linear profile showing measurement of length and thickness of the nanosheet. (b) The length and thickness sizing of C3 and C8 nanosheets. Arrow indicating increasing L_{NS} and reducing t_{NS} with larger ion chain sizes (c) Histogram of counts for the nanosheet length of the C8 sample with overlaid log-normal fit. (d) Histogram of counts for nanosheet thickness for the C8 sample with overlaid log-normal fit. (e−g) Mean nanosheet length, $< L_{NS}>$, mean nanosheet thickness, $< t_{NS}>$, and calculated mean aspect ratio, $< k_{NS}>$, as a function of ion chain length, n, respectively. (h) Mean nanosheet thickness as a function of mean nanosheet length. The dashed line in g illustrates n^2 dependence.

together, these data are a strong indicator that increasing ion size yields thinner nanosheets.

The absence of J2 and J3 vibrational modes in the Raman spectra, which are attributed to the metallic 1T phase, in Figure 1e provides further confirmation of the presence of the semiconducting 2H phase.[35,36] Figure S2 summarizes the Raman peak positions of both the $E_{2g}{}^1$ and A_{1g} modes of all inks. Interestingly, the $E_{2g}{}^1/A_{1g}$ intensity ratio increases with ion size (Figure 1e inset). According to our spectroscopic data (confirmed below via AFM), this implies that the $E_{2g}{}^1/A_{1g}$ intensity ratio increases with decreasing nanosheet thickness. However, for mechanically exfoliated MoS_2, the $E_{2g}{}^1/A_{1g}$ intensity ratio decreases with decreasing nanosheet thickness.[37] This contradiction may be from multiple sources. It may indicate the higher density of basal defects created during the exfoliation process using larger intercalating ions.[38] Similar behavior has also been observed in graphite exfoliation assisted by CO_2.[39] Alternatively, it may be because the presence of exfoliation debris (residual solvent, polymer, etc.) results in a dielectric environment that is different for liquid- versus mechanically exfoliated nanosheets, leading to subtle changes in Raman peak intensities. In Figure 1f, the blue shift (vibration stiffening) of the $E_{2g}{}^1$ mode and red shift (vibration softening) of the A_{1g} mode can be observed, which indicates more complete exfoliation and decreasing average thickness with increasing ion size.[37,40] Comparing this to spectra from the literature of unexfoliated MoS_2 crystal with much greater peak spacing (≈ 27 cm^{-1}) or our own measurement of ≈ 26 cm^{-1} (Figure S2) further demonstrates strong exfoliation of the crystal.[41]

The exfoliated material was examined using AFM to verify successful exfoliation of nanosheets, as shown in Figure 1g. The images show the production of larger lateral size and reduced thickness material for C8 compared to C3. TEM was performed on nanosheets to assess the morphology and crystalline quality of MoS_2 nanosheets following the EE process (Figure 1h). Through high-angle annular dark-field scanning transmission electron microscopy (HAADF-STEM) imaging, the nanosheets in C3 and C8 had lateral sizes on the order of micrometers with mostly smooth basal surfaces (Figure S3). From relative differences in the HAADF-STEM image brightness, we observed that the C8 nanosheets were thinner than those of C3, despite both exhibiting large lateral sizes. Distinct hexagonal spots visible in the selected area electron diffraction patterns provided confirmation of single-crystalline 2H phase MoS_2 nanosheets with edges primarily cleaved along the zigzag direction. Despite the high aspect ratios seen in C8, there is minimal wrinkling and folding of the nanosheet with sharp, clear edges compared with that of C3. The clean and crystalline edges visible in the HRTEM images demonstrated retention of the high crystalline quality of the nanosheets with minimal damage to the edges due to the gentle exfoliation process (5 min sonication).

Nanosheet Size Statistics

While the spectroscopic data imply that the nanosheets get thinner as ion size is increased, extensive AFM statistics are required to provide definitive proof and to verify nanosheet size control by alkylammonium ion choice. AFM was used to generate micrographs of nanosheets, as shown in Figure 2a. For each nanosheet, linear profiles along the long axes were used to extract dimensions: the lateral size (L_{NS}) was taken as the profile length, while the apparent thickness was determined by averaging the height measurements from each profile. This apparent thickness was then converted to layer number using previously reported step height analysis[42] and then converted to real nanosheet thickness, t_{NS}, by multiplying the layer number by the crystallographic thickness of MoS_2 (0.615 nm[43]). Profiles were measured and analyzed for around 100 nanosheets in each sample. Figure 2b shows a scatter plot of

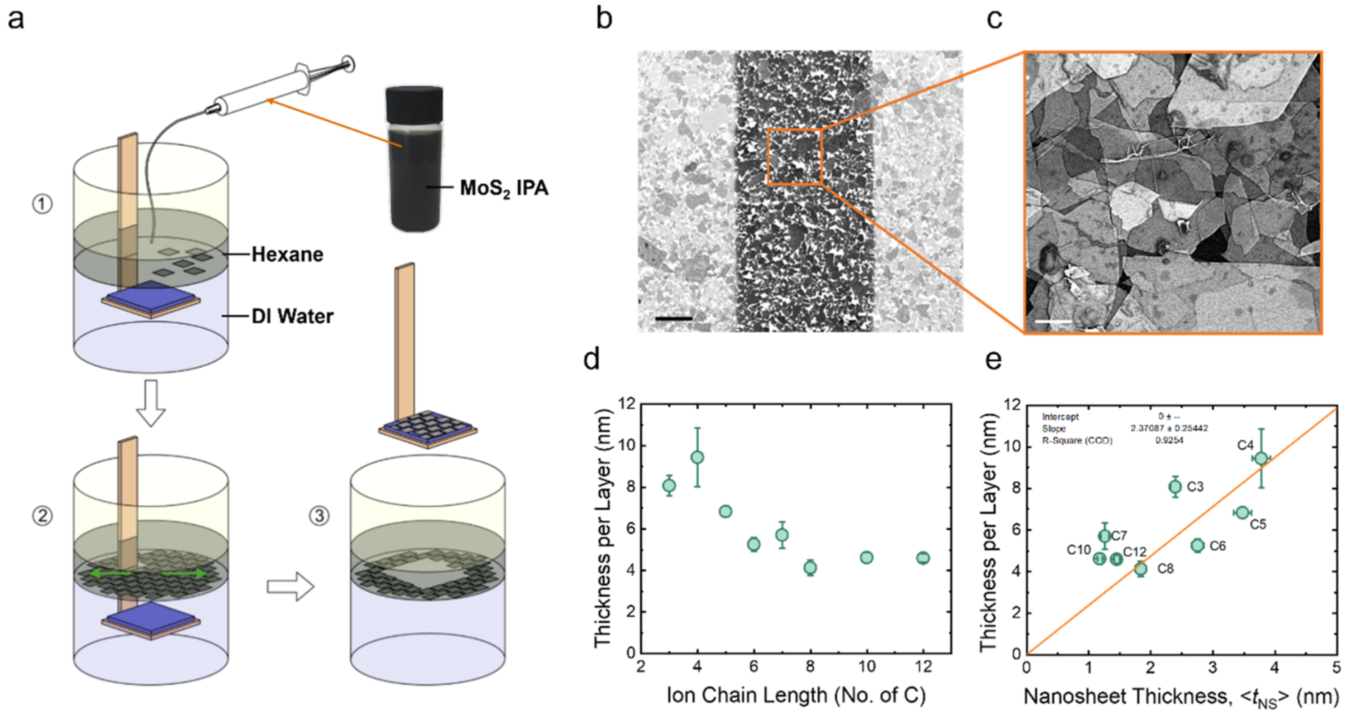

Figure 3. Deposition and characterization of thin MoS2 films. (a) Schematic of the deposition of thin films. Step 1 is the deposition of MoS_2 nanosheets in the water-hexane interface. Step 2 shows the spread and alignment of nanosheets parallel to the interface, causing the compression of nanosheets against the edges of the container, as indicated by the green arrows. Step 3 is the liftoff of the substrate through the interface, depositing the closed film on the substrate. (b) Low-resolution SEM image showing edge-to-edge aligned C8 nanosheets across gold contacts with single-layer deposition. Scale bar 20 μm. (c) Higher resolution SEM image of a single-layer MoS_2 film. Scale bar 10 μm. (d) Thickness per layer of films plotted versus ion chain length. (e) The network thickness per layer as a function of thickness (t_{NS}) of deposited nanosheets. This indicates that each layer is approximately two nanosheets thick.

L_{NS} vs t_{NS} for C3 and C8, with the arrow showing increasing L_{NS} and decreasing t_{NS} with increasing ion size. We note that the thinnest nanosheets observed are approximately 0.6 nm thick, consistent with clean monolayers. Example histograms showing L_{NS} and t_{NS} for C8 are shown in Figure 2c and d, respectively. These follow a log-normal distribution typical of size statistics for similar material.[19]

From histograms such as those in Figure 2c,d, (full histograms of L_{NS} and N shown in Figures S4 and S5, respectively) the mean nanosheet length and thickness, $< L_{NS}>$ and $< t_{NS}>$, were calculated for each sample. This data are plotted versus ion chain length, *n*, in Figure 2e,f. The nanosheet length is seen to increase with intercalating size, from the C3 ion's $< L_{NS}> = 1198 \pm 62$ nm to the C12 ion's $< L_{NS}> = 2838 \pm 123$ nm. Additionally, the nanosheet thickness was the largest for C4 with $< t_{NS}> = 3.8 \pm 0.1$ nm, and the smallest for C10 with $< t_{NS}> = 1.2 \pm 0.1$ nm. This leads to a trend of increasing mean aspect ratio (k_{NS}) with the size of the intercalating ion, with aspect ratio increasing from $< k_{NS}> = 500 \pm 24$ for C3 to $< k_{NS}> = 2333 \pm 120$ for C10. This demonstrates that increasing the size of the intercalating ion used yields larger, thinner nanosheets in electrochemical exfoliation (Figure 2h), in line with the spectroscopic results.

We can begin to understand the dependence of nanosheet dimensions on ion size as follows. We have previously shown that, for nanosheets produced by liquid exfoliation, in the ideal case the aspect ratio is given by $k_{NS} \propto E_{IP}/E_{OOP}$, where E_{IP} is the energy required (per unit area) to tear a nanosheet and E_{OOP} is the energy required (per unit area) to separate two nanosheets stacked on top of each other by van der Waals interactions.[19] The van der Waals energy of attraction between two nanosheets scales with their separation, D, as $V_{vdW} \propto -1/D^4$.[44] N.B. the exponent differs from the interatomic value of 6 due to the effect of adding large numbers of pairwise interatomic interactions.[45] Ion intercalation results in the increase in intermonolayer separation from the normal value to a value which we can approximate by the ion size, *d*. Here, the ion size is determined by the number of carbons in the side groups, *n*. Due to bond rotations, these groups will follow a roughly random walk geometry, allowing us to approximate: $d \propto n^{1/2}$.[46] Then the energy to separate to infinity two sheets initially separated by a distance *d* is $E_{OOP} = V_{vdW}(D = \infty) - V_{vdW}(D = d)$. This means $E_{OOP} \propto 1/d^4$. We note that we expect E_{IP} to be independent of *n*. Combining these results yields $k_{NS} \propto n^2$. We have superimposed this n^2 behavior on Figure 2g, finding reasonable agreement with the experimental data, although the scatter inherent to AFM measurements means alternative functions cannot be ruled out. Nonetheless, the consistency with the theoretically derived n^2 dependence suggests that ion intercalation significantly weakens intersheet binding, leading to higher aspect ratio flakes after exfoliation.

Film Deposition and Morphological Characterization

These nanosheets typically find applications in areas such as printed electronics in the form of printed thin films of nanosheets.[2] It is therefore necessary to fabricate such films and assess their electrical performance. To achieve conformal networks of these nanosheets and to minimize wastage of ink, we have used a liquid−liquid interface deposition technique to deposit nanosheets on substrates for electronic testing.[14,47] As illustrated in Figure 3a, when nanosheets are deposited at the

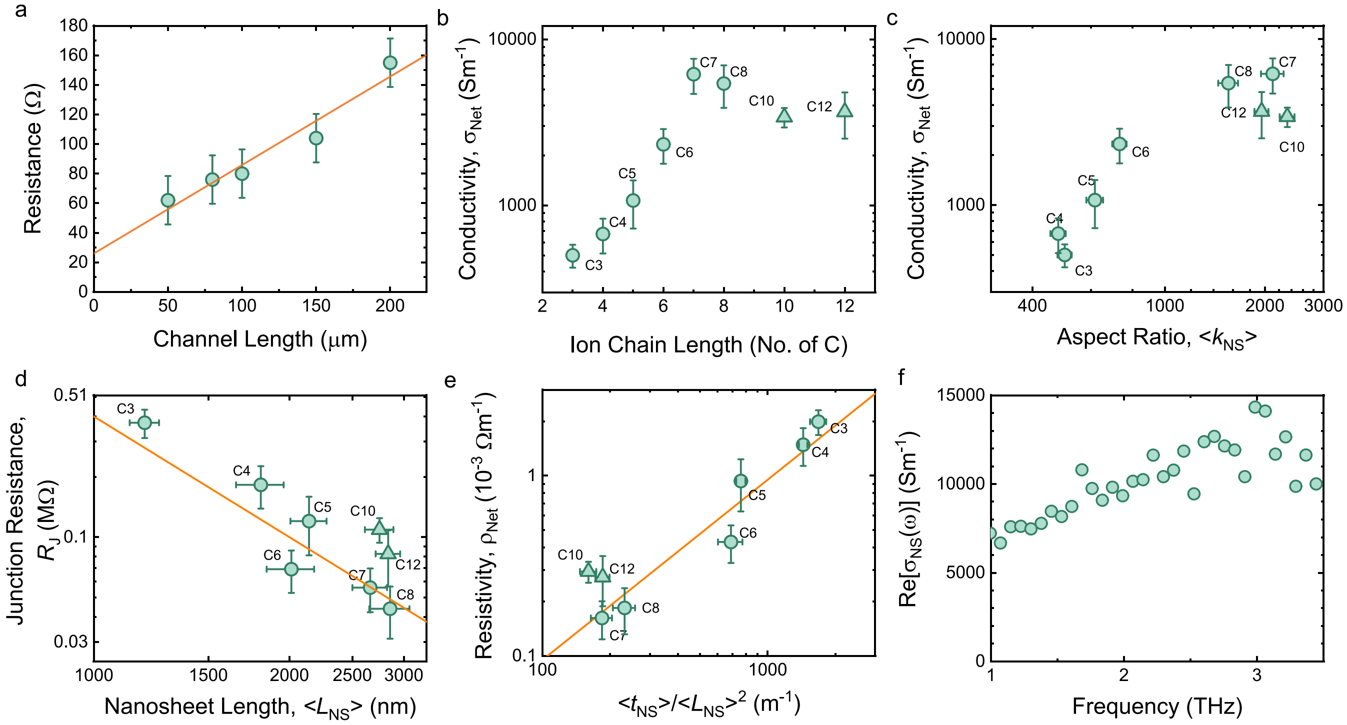

Figure 4. Electrical characterization of thin films. (a) Transmission Line Method plot to extract contact resistance and conductivity of measured samples. (b) Conductivity of film as a function of ion chain length. (c) Conductivity as a function of mean aspect ratio. (d) Calculated Junction Resistance (R_J) as a function of mean nanosheet length. (e) Conductivity as a function of t_{NS}/L^2. (f) Terahertz Time-Domain Spectroscopy showing optical conductivity plotted versus frequency.

interface of water and hexane, the interfacial tension between the two liquids causes nanosheets to align, yielding a highly conformal network.[14,47] SEM images of a single-layer film (Figure 3b, c) reveal a high degree of in-plane alignment of the nanosheets. All imaging was performed on a single-layer deposition for clarity. All electrical measurements were conducted on 3-layer films. This was to ensure networks were at least 10 nm thick to ensure sufficient network connectivity and to avoid percolation effects, which would dominate the conductivity of networks <5 nm thick.[14]

In order to facilitate electrical characterization, bottom contacts (100 nm gold with a 2 nm Ti bonding layer) were deposited on glass. Interdigitated electrodes (IDEs) with a width of 19 mm and channel lengths varying between 40 and 250 μm were used to enable contact resistance correction.[48] In all cases, three complete nanosheet layers were deposited to create a fully connected nanosheet network,[14,48] followed by annealing at 120 °C for 1h in an inert N_2 environment. Film thicknesses were measured by using White Light Interferometry (WLI), with the network thicknesses per layer shown in Figure 3d. The film thickness per layer is plotted versus the nanosheet thickness (measured by AFM) in Figure 3e. This shows that each layer is approximately two nanosheets thick on average.

Electrical Characterization

Finally, devices made from each ink were characterized using a probe station in an inert environment to reduce variations in device properties. In ambient conditions, film conductivities can fluctuate rapidly from changes in humidity,[49] light,[50] and atmospheric gases.[51] The in-plane resistance for each sample was measured as a function of the channel length. From this, the contact resistance was extracted using the Transmission Line Method (TLM),[52] with an example for C7 shown in Figure 4a. The network conductivity, σ_{Net}, for each film was calculated and plotted versus the ion size in Figure 4b. We note that on this graph, we have differentiated between samples (C3−C8), which were prepared using a one-step intercalation process, from those made using a two-step intercalation process (C10−C12). This graph shows that σ_{Net} increases with increasing ion size, reaching a maximum at C7, after which it falls off slightly.

It is likely that the apparent dependence of network conductivity on ion size is a reflection of the change in nanosheet dimensions with ion size observed in Figure 2. For example, a strong scaling of conductivity with aspect ratio is observed in Figure 4c, indicating that the nanosheet size has a crucial impact on the electrical properties of the nanosheet network. This scaling appears to apply between C3 and C8, while C10 and C12 show lower conductivity than expected given their aspect ratio. This indicates that although nanosheet dimensions play a pivotal role in dictating electrical conduction through nanosheet networks, the nature of the intercalation procedure (one-step versus two-step) also plays a role.

In order to understand the factors limiting conductivity in these networks, we apply a recently published network conduction model.[11] This model can be simplified to represent networks of nanosheets with moderate to high carrier density, such that the network conductivity is given by

$$\sigma_{Net} = \frac{(1 - P_{Net})}{\rho_{NS} + 2t_{NS}R_J} \qquad (1)$$

where P_{Net} is the network porosity, ρ_{NS} is the nanosheet resistivity, t_{NS} is the mean nanosheet thickness, and R_J is the junction resistance (for neatness, we neglect the < > symbols indicating means in the equations in this paper). We note that this model has been shown to accurately describe the electrical properties of networks of graphene, WS_2, and WSe_2 nanosheets with low aspect ratio produced by liquid phase exfoliation,[11] networks of high aspect ratio graphene and MoS_2 nanosheets produced by electrochemical exfoliation,[9] as well as networks of silver nanowires[11,53] and nanoplatelets.[11]

In almost all cases, networks are limited by transport across internanosheet junctions such that the nanosheet resistance is much smaller than the junction resistance. Under these circumstances, $\rho_{NS} < < 2t_{NS}R_J$, allowing us to rewrite eq 1: $R_J \approx (1 - P_{Net})/2t_{NS}\sigma_{Net}$. Then, using the measured values of t_{NS} and an estimated value of $P_{Net} = 10\%$ (reasonable for networks of electrochemically exfoliated nanosheets), we convert our network conductivity values to approximate junction resistance values, with R_J plotted versus mean nanosheet length ($<L_{NS}>$) in Figure 4d. We find a clear trend of reducing R_J with increasing $< L_{NS}>$ for the one-step samples (C3−C8), with the two-step samples (C10−C12) lying slightly above the trendline.

It is known that higher aspect ratio nanosheets tend to bend and conform to one another, creating highly aligned contacts between nanosheets at the internanosheet junctions.[9] It is likely that larger nanosheets achieve greater overlap when stacked, giving a junction area that scales with nanosheet area, i.e., $A_J = fL_{NS}^2$, where f is a constant which is ∼ 0.25.[9] We propose that the junction resistance scales with junction area as $R_J = (RA)_J/A_J = (RA)_J/fL_{NS}^2$ where $(RA)_J$ is a constant that quantifies internanosheet sheet charge transfer. This equation is consistent with the behavior seen in Figure 4e. Fitting the C3−C8 data using this model finds very good agreement with $(RA)_J/f = 4 \pm 0.4 \times 10^{11}\ \Omega m^2$. Estimating f = 0.25 gives $(RA)_J = 1.0 \pm 0.1 \times 10^{11} \Omega m^2$. This compares to recently estimated values of $1.3 \pm 0.1 \times 10^{11} \Omega m^2$, and $1.6 \pm 0.1 \times 10^{11} \Omega m^2$ for electrochemically exfoliated MoS_2 networks.[11,54] We note that the fact that all of the C3−C8 data points lie close to the fit line implies that all of these networks have very similar values of $(RA)_J/f$. This in turn implies that neither exposure to the ions during intercalation nor the presence of residual adsorbed ions in the network results in modifications in junction resistance that scale with ion size. Furthermore, because $(RA)_J$ has been observed to scale with the ρ_{NS},[11] this suggests no significant ion size-dependent impact on ρ_{NS}.

We can use this relationship between junction resistance and nanosheet size to rewrite eq 1 in terms of the network resistivity and nanosheet dimensions

$$\rho_{Net} \approx \frac{1}{(1 - P_{Net})}\left[\rho_{NS} + \frac{2(RA)_J t_{NS}}{fL_{NS}^2}\right] \tag{2}$$

This implies that the nanosheet resistivity scales linearly with $< t_{NS}>/ < L_{NS}>^2$. As shown in Figure 4e, we find this to be approximately the case, excluding the C10 and C12 samples. However, we find that the scatter is such that we cannot accurately identify the intercept and so cannot quantify the nanosheet resistivity.

As indicated above, the electrical resistivity is higher for ions larger than C8. This is at least partly because of the higher junction resistances, as indicated in Figure 4d, but may also be due to increased nanosheet resistivity. PL/Raman analysis indicates that larger ions and the preintercalation step are impacting material quality as seen by changes in the PL/Raman spectra described in Figure 1c and d, which are attributed to defects generated in the basal plane. These changes in material quality impact the electronic properties of the nanosheet networks, reducing the network conductivity for C8 and particularly for C10 and C12.

Terahertz time-domain spectroscopy (THz-TDS) was performed to extract nanosheet electronic data parameters for a film of C8 nanosheets. Measurements were taken in various positions on the film, yielding similar results. A representative spectrum is shown in Figure 4f. This data show relatively low frequency dispersion with THz conductivity values between 7,000 and 14,000 S/m. Averaging over multiple films yields a mean THz conductivity of 10800 ± 1500 S/m. Assuming this is a reasonable proxy for the DC conductivity of the nanosheets themselves allows us to estimate $\rho_{NS}{\sim}10^{-4}$ Ωm. This value is consistent with nanosheet mobilities of ∼60 $cm^2/(V\ s)$ and carrier densities of $\sim 10^{25}\ m^{-3}$, which are reasonable for EE MoS_2.[11,14] This implies the presence of residual ions to not significantly alter the electrical properties of individual nanosheets. In addition, the closeness of this value to our lowest ρ_{Net} shows the electrical properties of our best networks (e.g., C7, $\rho_{Net} \approx 1.7 \times 10^{-4}\ \Omega m$, $\sigma_{Net} \approx 6000$ S/m) are approaching those of the nanosheets themselves. We emphasize that these high-conductivity networks are facilitated by low-resistance junctions, which are in turn associated with large area, very thin nanosheets.

We believe that controlling the size of intercalated alkylammonium ions is an important tool to control the properties of printed networks and their devices. Intercalating these ions increases the interlayer spacing during intercalation via their steric volume, reducing the van der Waals attraction between adjacent monolayers and thereby facilitating complete separation during exfoliation. This enlarged spacing, together with residual surface-bound ions, also helps suppress restacking during exfoliation and ink formulation by maintaining larger effective separation distances between the nanosheets. Because junction resistance is highly sensitive to nanosheet geometry and overlap area, this ion-driven control over nanosheet length and thickness acts as a form of "junction engineering": larger, thinner nanosheets generated by larger ions form wider, more conformal contacts that reduce R_J, whereas smaller ions produce shorter, thicker nanosheets that lead to smaller junction areas and higher junction resistance. Thus, ion selection indirectly governs the junction resistance by dictating nanosheet dimensions and junction morphology in printed networks.

■ CONCLUSION

In this work, we demonstrated that the alkylammonium ion size serves as a critical parameter for controlling the size and electrical properties of electrochemically exfoliated MoS_2 nanosheets. By tailoring the intercalant ion, we achieved precise tuning of nanosheet lengths (L_{NS} = 1−3 μm) and aspect ratios (k_{NS} = 400−2500). Additionally, we found that networks of these dimension-controlled nanosheets demonstrate a strong dependence of network conduction on both nanosheet aspect ratio and $< t_{NS}>/<L_{NS}>^2$. This confirms that larger, thinner nanosheets have reduced junction resistances, in agreement with theoretical models of flake-to-flake junction resistance.

This work highlights the importance of the alkylammonium ion choice in the electrochemical exfoliation process. It also shows the importance of nanosheet dimensions in maximizing the electrical performance of nanosheet networks. Both factors

https://doi.org/10.1021/acsami.5c24890

should serve as a guide to future work in the electrochemical exfoliation of 2D materials, as well as optimizing electronic conduction through networks of 2D materials in printed electronics. These insights provide a roadmap for creating printed electronics: for applications requiring high conductivity, such as gas sensors, strain gauges, and flexible electronics, our results recommend using larger ions (C8−C12) to produce large, thin nanosheets that minimize junction resistance, a primary bottleneck in network devices. Shorter, thicker nanosheets (C3−C6) will form higher porosity networks with more exposed nanosheet edges, making them superior candidates for applications as electrochemical sensors, battery electrodes, or photocatalytic systems.

The strategy of ion-selected exfoliation may also be transferable to other semiconducting transition metal dichalcogenides (e.g., WS_2, $MoSe_2$) for tailoring their nanosheet and network properties. Ultimately, by linking quaternary ion selection to nanosheet geometry and network performance, this work provides a roadmap for designing high-performance, solution-processed 2D material devices.

METHODS

Electrochemical Exfoliation

A thin piece of MoS_2 crystal was cleaved from an as-received crystal (Sofer Group, UCT Prague) to be used as the cathode during electrochemical exfoliation. Platinum foil (Alfa Aesar) was used as the anode. Small copper crocodile clips were used to hold the electrodes in place. The chosen alkylammonium ion was dissolved in 40 mL of either propylene carbonate (PC) or acetonitrile (ACN) to prepare the electrolyte. For smaller ions (C3−C6), a 3 g/L solution was prepared in PC, while for intermediate-sized ions (C7 and C8), a 3 g/L solution was prepared in ACN. A constant potential of 7 V was then applied across the working and counter electrodes for 30 min to intercalate the MoS_2 crystal. For the largest ions (C10 and C12), a two-step intercalation process was employed: first, the MoS_2 was preintercalated using 1 g/L C7 in ACN at 7 V for 20 min, followed by a second intercalation step with 3 g/L of either C10 or C12 in ACN under identical conditions. In all cases, the electrolyte turned yellow, and the presence of Br^- indicated that intercalation of ions into the material was occurring. The MoS_2 crystal expanded to many times its original volume after 30 min, indicating successful intercalation of the crystal.

The solvent was drained off, and the expanded material was added to 30 mL of 1 g/L poly(vinylpyrrolidone) (PVP, molecular weight ∼40,000) in dimethylformamide (DMF). This was bath ultrasonicated for 5 min to complete exfoliation of the material. The resulting dispersion was then centrifuged (Hettich Mikro 220R, 1195-A, radius 87 mm) at 24 g for 30 min to remove unexfoliated material. To remove the PVP, the 24 g of supernatant was redispersed in 30 mL of DMF and was centrifuged at 3824 g for 60 min. This was repeated. The resulting sediment was then redispersed in IPA and centrifuged at 3824 g for 60 min. The final sediment was then redispersed in IPA again, giving the cleaned dispersion.

Thin Film Deposition

Masks with interdigitated electrodes (IDEs) were attached to 2 × 2 cm^2 glass with channel lengths of 50, 80, 100, 150, and 200 μm. 80 nm of gold and 10 nm of Cr as an adhesion layer were evaporated onto the mask and substrate using a Temescal DC-2000 system to create bottom contacts.

Cleaned substrates were required for the deposition of thin films. Substrates were sonicated in acetone, purified water, and IPA for 10 min each. This removed residue or debris on the substrates, which would disrupt film deposition.

Films were deposited using a dip coater setup, as published recently.[14] 40 mL of deionized (DI) water were added to a 50 mL beaker. The substrate was then mounted on a dip coater, and the substrate was then slowly (1 mm/s) lowered into the beaker of DI water. 2 mL of hexane was added, creating a liquid−liquid interface. A stirrer was added, and the beaker was stirred gently throughout the process to ensure a uniform spread of the nanosheets across the interface. The ink was loaded into a 5 mL syringe and then fitted into a syringe pump. The injection rate was initially set to 60 μL/min and then slowed to 20 μL/min when the film began to compress. When the film had become fully compressed and homogeneous, the substrate was slowly lifted from the beaker at a rate of 1 mm/s using the dip coater. The film was allowed to dry at room temperature for 30 min, before being annealed at 40 °C for 1 h to dry fully. This process was then repeated twice, giving three-layer films. The three-layer films were then annealed at 120 °C in an argon environment. While trace amounts of PVP and organic residue remain after annealing and washing steps,[55] the consistent protocol across all samples ensures any residual organic content is relatively constant. Moreover, films in the bulk regime (>10 nm) have their transport dominated by internanosheet junctions rather than residues on the nanosheets.[9,11]

Electrical Measurements. Electrical characteristics were measured in an argon environment by using a Keithley 2612A source meter connected to a probe station. Extracted resistances were plotted versus IDE channel lengths, with the TLM method used to extract contact resistance from the intercept. The slopes of these plots were then used to calculate the conductivity of each sample. TLM plots for each sample are seen in S7

Material Characterization

Atomic Force Microscopy (AFM). A Bruker Multimode 8 scanning probe microscope was used in ScanAsyst mode (non-contact) in air under ambient conditions using aluminum-coated silicon cantilevers (OLTESPA-R3). Substrates for AFM were coated with (3-Aminopropyl)triethoxysilane (APTES) by soaking them in a solution of APTES and deionized water for 15 min. Substrates were then removed and washed by rinsing with deionized water and pressurized nitrogen repeatedly. Inks as used for films were deposited on APTES-coated SiO2 wafers (5 × 5 mm^2). A single drop of the dispersion (10 μL) was dropped onto the prepared substrate, held for 30 s, and then blown off with pressurized nitrogen. The sample was then rinsed with water, followed by isopropanol, which was then blown off with pressurized nitrogen. This prevents solvent airdrying on the substrate, creating the coffee ring effect. This process was then repeated with further drops of dense coverage of nanosheets across the sample that could be seen under an optical microscope. AFM scan sizes of between 15 × 15 and 30 × 30 μm^2 were used for shorter and longer nanosheet samples, respectively. Scan rates between 0.35 and 0.7 Hz were used, taking either 512 or 1024 lines per image for smaller or larger images, respectively. Respective images for each sample can be found in S6.

AFM Statistics. To extract quantitative data on nanosheet sizing of each sample, AFM statistics were carried out on the AFM images. Linear profiles were extracted for imaged nanosheets along the longest axis (the length), and from these, the thickness of the nanosheet was also measured. Nanosheet thickness measurements by AFM are typically offset due to the tip−sample effects as well as residues around the nanosheets. We correct for these effects via step height analysis using previous AFM measurements of MoS_2 step height as 1.9 nm.[42] This height is generally considered to represent the measured monolayer thickness with deviations from expectations due to the aforementioned tip−sample and residue effects. The nanosheet's apparent thickness was converted to the layer number by dividing the apparent thickness by this step height. From the layer number, the real thickness, t_{NS}, was calculated using a crystallographic thickness of 0.615 nm for MoS_2.[43] However, we note that this approach cannot fully eliminate the effects of organic residues and may be expected to lead to a small systematic error. To account for the disproportionate contribution of larger nanosheets to network properties, the volume-weighted mean layer number was calculated as

$$<N>_V = \frac{\sum_i N_i \cdot V_i}{\sum_i V_i} \tag{3}$$

where N_i is the layer number and V_i is the volume of each nanosheet. This was used to obtain the mean thickness, $\langle t_{NS} \rangle$, for each sample. The mean nanosheet length $\langle L_{NS} \rangle$ was calculated as the arithmetic mean of the measured lengths.[42]

Optical Absorption Spectroscopy. The spectra of nanosheet dispersions were collected by Lambda spectrometer from 900 to 200 nm with a 1 nm step and 2 nm slit width. The dispersion was placed in a 10 mm long optical length cuvette. The absorption spectra were collected in an integrating sphere. The solvent spectra were subtracted from the collected extinction and absorption spectra of nanosheet dispersions to yield only nanosheet spectra for each. The scattering spectra were obtained by subtracting the absorption from the extinction spectra.

Photoluminescence (PL) and Raman spectroscopy. Raman and PL data for MoS_2 nanosheet films were collected in a Renishaw Invia system equipped with a ×50 objective. A 532 nm laser source was used and the power of the laser was kept under ∼1 mW to avoid damage to the sample. The exposure time was 10, and 10 spectra at different spots of each sample were collected for averaging the data. The collection range was 534 to 800 nm (2.32 eV to 1.55 eV). All PL/Raman data were fitted to a Lorentzian. The films were deposited on glass via Langmuir−Schaffer deposition.

Scanning Electron Microscopy. SEM imaging was conducted using a Carl Zeiss Ultra SEM. A secondary electron detector was used to obtain the images at a 3 kV accelerating voltage, 5 mm working distance, and 30 μm aperture.

Transmission Electron Microscopy (TEM) Sample Preparation. A drop was placed on a lacey carbon copper TEM grid. The TEM grid was then placed in a Coors alumina boat within a quartz glass tube (27 mm inner diameter and 28 mm outer diameter) in a Thermo Scientific Lindberg Blue M Mini-Mite tube furnace. The tube was purged with 500 sccm of argon−hydrogen (15% H2) gas. The flow was reduced to 200 sccm, and the furnace was heated to 300 °C (ramp: 15 °C/min) and held for 1 h. The furnace was cooled naturally to room temperature in flowing argon−hydrogen gas before removing the TEM grid.

TEM Instrumentation. Imaging was performed in a FEI Talos F200X equipped with a cold field emission gun operated at 200 kV. Selected area electron diffraction (SAED) was acquired using a 40 μm diameter aperture. Bright-field (BF-) and off-axis dark-field (DF-) TEM imaging was acquired by placing a 15 μm diameter aperture on the transmitted beam (BF-TEM) or diffracted spot (DF-TEM). High-angle annular dark-field scanning transmission electron microscopy (HAADF-STEM) images were acquired using an annular detector with a collection angle of 42−244 mrad, camera height of 115 mm, and convergence angle of 30 mrad. Energy dispersive X-ray spectroscopy (EDS) was acquired in STEM mode by using a Super-X detector. Fast Fourier Transform (FFT) analysis was performed by using DigitalMicrograph software. EDS maps were analyzed and generated by using Thermo Fisher Scientific Velox Software.

Terahertz Time-Domain Spectroscopy (THz-TDS). The samples were half-covered during measurements such that the uncovered half serves as an on-chip reference, eliminating realignment errors when the optical path was switched between the sample and reference. THz transmission measurements were carried out in a nitrogen atmosphere inside a purge box with a THz spectrometer driven by a 90 fs pulsed 1.55 μm, 100 MHz Er-doped fiber laser (Menlo Systems). The laser delivered an ≈20 mW average power to both the photoconductive emitter and detector antennas (Menlo Systems). Time-resolved THz transients from both the sample and the on-chip reference were recorded. To suppress internal Fabry−Perot echoes of the 1.5 mm quartz, a simple time gate was applied that removed the first reflection. Fast Fourier transformation yields the complex transmission spectrum, which was converted to sheet conductivity $\sigma(\omega)$ with Tinkham's thin-film equation. Volume conductivity was obtained by dividing σ by the physical film thickness of 8.3 nm, as obtained from atomic force microscopy at a scratch in the MoS2 film.

■ ASSOCIATED CONTENT

Supporting Information

The Supporting Information is available free of charge at https://pubs.acs.org/doi/10.1021/acsami.5c24890.

> UV/vis extinction, absorption, and scattering spectra for all samples; raman spectra for all samples; HAADF-STEM morphological assessment; nanosheet length and layer number histograms; representative AFM images of each sample; and resistance as a function of channel length for each sample (PDF)

■ AUTHOR INFORMATION

Corresponding Author

Jonathan N. Coleman − *School of Physics, CRANN & AMBER Research Centres, Trinity College Dublin, Dublin 2, Ireland;* orcid.org/0000-0001-9659-9721; Phone: +353 (0) 1 8963859; Email: colemaj@tcd.ie

Authors

Anthony Dawson − *School of Physics, CRANN & AMBER Research Centres, Trinity College Dublin, Dublin 2, Ireland*

Vincent Renard − *School of Physics, CRANN & AMBER Research Centres, Trinity College Dublin, Dublin 2, Ireland*

Weimiao Wang − *School of Physics, CRANN & AMBER Research Centres, Trinity College Dublin, Dublin 2, Ireland*

Tian Carey − *School of Physics, CRANN & AMBER Research Centres, Trinity College Dublin, Dublin 2, Ireland;* orcid.org/0000-0001-8697-9421

Rebekah Wells − *School of Physics, CRANN & AMBER Research Centres, Trinity College Dublin, Dublin 2, Ireland*

David Sanchez − *Department of Materials Science and Engineering, Pennsylvania State University, University Park, Pennsylvania 16802, United States*

Joseph Neilson − *School of Physics, CRANN & AMBER Research Centres, Trinity College Dublin, Dublin 2, Ireland;* orcid.org/0000-0002-2472-4869

Jack Doran − *School of Physics, CRANN & AMBER Research Centres, Trinity College Dublin, Dublin 2, Ireland*

Eoin Caffrey − *School of Physics, CRANN & AMBER Research Centres, Trinity College Dublin, Dublin 2, Ireland;* orcid.org/0000-0002-0174-383X

Cian Gabbett − *School of Physics, CRANN & AMBER Research Centres, Trinity College Dublin, Dublin 2, Ireland*

Paul Seifert − *Institute of Physics, EIT 2, Faculty of Electrical Engineering and Information Technology, Universität der Bundeswehr München, 85577 Neubiberg, Germany*

Martin Gerlei − *Institute of Physics, EIT 2, Faculty of Electrical Engineering and Information Technology, Universität der Bundeswehr München, 85577 Neubiberg, Germany;* orcid.org/0009-0007-3960-7458

Georg Duesberg − *Institute of Physics, EIT 2, Faculty of Electrical Engineering and Information Technology, Universität der Bundeswehr München, 85577 Neubiberg, Germany;* orcid.org/0000-0002-7412-700X

Mauricio Terrones − *Department of Materials Science and Engineering, Pennsylvania State University, University Park, Pennsylvania 16802, United States; Department of Physics and Chemistry, Pennsylvania State University, University*

Park, Pennsylvania 16802, United States; orcid.org/0000-0003-0010-2851

Zdenek Sofer − Department of Inorganic Chemistry, University of Chemistry and Technology Prague, Prague 6 166 28, Czech Republic; orcid.org/0000-0002-1391-4448

Kevin Synnatschke − Center for Advancing Electronics Dresden (cfaed) and Faculty of Chemistry and FoodChemistry, Technische Universität Dresden, 01062 Dresden, Germany

Complete contact information is available at: https://pubs.acs.org/10.1021/acsami.5c24890

Notes

The authors declare no competing financial interest.

ACKNOWLEDGMENTS

We acknowledge the Horizon Europe project 2D-PRINTABLE and Taighde Éireann − Research Ireland under Grant number RI-23/FFP-A/12254. We have also received support from the Research Ireland-funded center AMBER and availed of the facilities of the Research Ireland-funded AML and ARL laboratories. A.D. appreciates support from Research Ireland (18/EPSRC-CDT/3581). K.S. acknowledges the financial support by Deutsche Forschungsgemeinschaft (DFG, German Research Foundation) through SFB 1415, Project A11 (project-ID 417590517).

REFERENCES

(1) Carey, T.; Cassidy, O.; Synnatschke, K.; Caffrey, E.; Garcia, J.; Liu, S.; Kaur, H.; Kelly, A. G.; Munuera, J.; Gabbett, C.; O'Suilleabhain, D.; Coleman, J. N. High-Mobility Flexible Transistors with Low-Temperature Solution-Processed Tungsten Dichalcogenides. *ACS Nano* **2023**, *17* (3), 2912−2922.

(2) Carey, T.; Arbab, A.; Anzi, L.; Bristow, H.; Hui, F.; Bohm, S.; Wyatt-Moon, G.; Flewitt, A.; Wadsworth, A.; Gasparini, N.; Kim, J. M.; Lanza, M.; McCulloch, I.; Sordan, R.; Torrisi, F. Inkjet Printed Circuits with 2D Semiconductor Inks for High-Performance Electronics. *Adv. Electron. Mater.* **2021**, *7* (7), No. 2100112.

(3) Mei, L.; Gao, Z.; Yang, R.; Zhang, Z.; Sun, M.; Liang, X.; Zhang, Y.; Ying, T.; Hu, H.; Li, D.; Zhang, Q.; Gu, M. D.; Gu, L.; Zhou, J.; Huang, B.; Voiry, D.; Zeng, X. C.; Chai, Y.; Li, J.; Yu, X.; Zeng, Z. Phase-Switchable Preparation of Solution-Processable WS2Mono- or Bilayers. *Nat. Synth.* **2025**, *4* (3), 303−313.

(4) Finn, D. J.; Lotya, M.; Cunningham, G.; Smith, R. J.; McCloskey, D.; Donegan, J. F.; Coleman, J. N. Inkjet Deposition of Liquid-Exfoliated Graphene and MoS2 Nanosheets for Printed Device Applications. *J. Mater. Chem. C* **2014**, *2*, 925−932.

(5) Gu, X.; Cui, W.; Li, H.; Wu, Z.; Zeng, Z.; Lee, S.-T.; Zhang, H.; Sun, B. A Solution-Processed Hole Extraction Layer Made from Ultrathin MoS2 Nanosheets for Efficient Organic Solar Cells. *Adv. Energy Mater.* **2013**, *3* (10), 1262−1268.

(6) Kong, S.; Wu, T.; Yuan, M.; Huang, Z.; Meng, Q.-L.; Jiang, Q.; Zhuang, W.; Jiang, P.; Bao, X. Dramatically Enhanced Thermoelectric Performance of MoS2 by Introducing MoO2 Nanoinclusions. *J. Mater. Chem. A* **2017**, *5* (5), 2004−2011.

(7) Nicolosi, V.; Chhowalla, M.; Kanatzidis, M. G.; Strano, M. S.; Coleman, J. N. Liquid Exfoliation of Layered Materials. *Science* **2013**, *340* (6139), No. 1226419.

(8) Kelly, A. G.; Hallam, T.; Backes, C.; Harvey, A.; Esmaeily, A. S.; Godwin, I.; Coelho, J.; Nicolosi, V.; Lauth, J.; Kulkarni, A.; Kinge, S.; Siebbeles, L. D. A.; Duesberg, G. S.; Coleman, J. N. All-Printed Thin-Film Transistors from Networks of Liquid-Exfoliated Nanosheets. *Science* **2017**, *356* (6333), 69−73.

(9) Caffrey, E.; Munuera, J. M.; Gabbett, C.; Doolan, L.; Neilson, J.; Wells, R. A.; McCrystall, M.; McNamara, A.; Carey, T.; Gerlei, M.; Seifert, P.; Duesberg, G. S.; Coleman, J. N. Quantifying the Influence of Nanosheet Aspect Ratio on Network Morphology and Junction Resistance in Solution-Processed Nanosheet Networks. *ACS Nano* **2025**, *19* (37), 33118−33133.

(10) Gabbett, C.; Doolan, L.; Synnatschke, K.; Gambini, L.; Coleman, E.; Kelly, A. G.; Liu, S.; Caffrey, E.; Munuera, J.; Murphy, C.; Sanvito, S.; Jones, L.; Coleman, J. N. Quantitative Analysis of Printed Nanostructured Networks Using High-Resolution 3D FIB-SEM Nanotomography. *Nat. Commun.* **2024**, *15* (1), No. 278.

(11) Gabbett, C.; Kelly, A. G.; Coleman, E.; Doolan, L.; Carey, T.; Synnatschke, K.; Liu, S.; Dawson, A.; O'Suilleabhain, D.; Munuera, J.; Caffrey, E.; Boland, J. B.; Sofer, Z.; Ghosh, G.; Kinge, S.; Siebbeles, L. D. A.; Yadav, N.; Vij, J. K.; Aslam, M. A.; Matkovic, A.; Coleman, J. N. Understanding How Junction Resistances Impact the Conduction Mechanism in Nano-Networks. *Nat. Commun.* **2024**, *15* (1), No. 4517.

(12) Kelly, A. G.; O'Suilleabhain, D.; Gabbett, C.; Coleman, J. N. The Electrical Conductivity of Solution-Processed Nanosheet Networks. *Nat. Rev. Mater.* **2022**, *7* (3), 217−234.

(13) Carey, T.; Synnatschke, K.; Ghosh, G.; Anzi, L.; Caffrey, E.; Coleman, E.; Lin, C.; Dawson, A.; Liu, S.; Wells, R.; McCrystall, M.; Plutnar, J.; Plutnarová, I.; Neilson, J.; Marzari, N.; Siebbeles, L. D. A.; Sordan, R.; Sofer, Z.; Coleman, J. N. Electronic Properties and Circuit Applications of Networks of Electrochemically Exfoliated 2D Nanosheets. *Nat. Commun.* **2025**, *16* (1), No. 9038.

(14) Neilson, J.; Caffrey, E.; Cassidy, O.; Gabbett, C.; Synnatschke, K.; Schneider, E.; Munuera, J. M.; Carey, T.; Rimmer, M.; Sofer, Z.; Maultzsch, J.; Haigh, S. J.; Coleman, J. N. Production of Ultrathin and High-Quality Nanosheet Networks via Layer-by-Layer Assembly at Liquid−Liquid Interfaces. *ACS Nano* **2024**, *18* (47), 32589−32601.

(15) Lin, Z.; Liu, Y.; Halim, U.; Ding, M.; Liu, Y.; Wang, Y.; Jia, C.; Chen, P.; Duan, X.; Wang, C.; Song, F.; Li, M.; Wan, C.; Huang, Y.; Duan, X. Solution-Processable 2D Semiconductors for High-Performance Large-Area Electronics. *Nature* **2018**, *562* (7726), 254−258.

(16) Zhao, M.; Casiraghi, C.; Parvez, K. Electrochemical Exfoliation of 2D Materials beyond Graphene. *Chem. Soc. Rev.* **2024**, *53* (6), 3036−3064.

(17) Yang, H.; Synnatschke, K.; Yoon, J.; Mirhosseini, H.; Hermes, I. M.; Li, X.; Neumann, C.; Morag, A.; Turchanin, A.; Kühne, T. D.; Parkin, S. S. P.; Yang, S.; Nia, A. S.; Feng, X. Solution-Processable Electronic-Grade 2D WTe2 Enabled by Synergistic Dual Ammonium Intercalation. *ACS Nano* **2025**, *19* (14), 14309−14317.

(18) Lin, Z.; Wan, Z.; Song, F.; Huang, B.; Jia, C.; Qian, Q.; Kang, J. S.; Wu, Y.; Yan, X.; Peng, L.; Wan, C.; Zhou, J.; Sofer, Z.; Shakir, I.; Almutairi, Z.; Tolbert, S.; Pan, X.; Hu, Y.; Huang, Y.; Duan, X. High-Yield Exfoliation of 2D Semiconductor Monolayers and Reassembly of Organic/Inorganic Artificial Superlattices. *Chem* **2021**, *7* (7), 1887−1902.

(19) Backes, C.; Campi, D.; Szydlowska, B. M.; Synnatschke, K.; Ojala, E.; Rashvand, F.; Harvey, A.; Griffin, A.; Sofer, Z.; Marzari, N.; Coleman, J. N.; O'Regan, D. D. Equipartition of Energy Defines the Size−Thickness Relationship in Liquid-Exfoliated Nanosheets. *ACS Nano* **2019**, *13* (6), 7050−7061.

(20) Zhang, J.; Wang, L.; Lü, J.; Wang, Z.; Wu, H.; Zhu, G.; Wang, N.; Xue, F.; Zeng, X.; Zhu, L.; Hu, Y.; Deng, X.; Guan, C.; Yang, C.; Lin, Z.; Wang, P.; Zhou, B.; Lü, J.; Zhu, W.; Zhang, X.; Huang, Y.; Huang, W.; Peng, Y.; Duan, X. Interlayer Reconstruction Phase Transition in van Der Waals Materials. *Nat. Mater.* **2025**, *24* (3), 369−376.

(21) Li, J.; Song, P.; Zhao, J.; Vaklinova, K.; Zhao, X.; Li, Z.; Qiu, Z.; Wang, Z.; Lin, L.; Zhao, M.; Herng, T. S.; Zuo, Y.; Jonhson, W.; Yu, W.; Hai, X.; Lyu, P.; Xu, H.; Yang, H.; Chen, C.; Pennycook, S. J.; Ding, J.; Teng, J.; Neto, A. H. C.; Novoselov, K. S.; Lu, J. Printable Two-Dimensional Superconducting Monolayers. *Nat. Mater.* **2021**, *20* (2), 181−187.

(22) Li, L.; Yu, X.; Lin, Z.; Cai, Z.; Cao, Y.; Kong, W.; Xiang, Z.; Gu, Z.; Xing, X.; Duan, X.; Song, Y. Interface Capture Effect Printing Atomic-Thick 2D Semiconductor Thin Films. *Adv. Mater.* **2022**, *34* (49), No. 2207392.

(23) Chen, L.; Parvez, K.; Nepa, F.; Dimaggio, E.; Dun, C.; Read, O.; Urban, J. J.; Fiori, G.; Casiraghi, C. Ionic-Liquid Free and Flexible Transistors Made of 2D Material Inks. *Small* **2025**, *21* (50), No. e08360.

(24) Yang, R.; Fan, Y.; Mei, L.; Shin, H. S.; Voiry, D.; Lu, Q.; Li, J.; Zeng, Z. Synthesis of Atomically Thin Sheets by the Intercalation-Based Exfoliation of Layered Materials. *Nat. Synth.* **2023**, *2* (2), 101−118.

(25) Peng, J.; Liu, Y.; Lv, H.; Li, Y.; Lin, Y.; Su, Y.; Wu, J.; Liu, H.; Guo, Y.; Zhuo, Z.; Wu, X.; Wu, C.; Xie, Y. Stoichiometric Two-Dimensional Non-van Der Waals AgCrS2 with Superionic Behaviour at Room Temperature. *Nat. Chem.* **2021**, *13* (12), 1235−1240.

(26) Grillo, A.; Parvez, K.; Wang, J.; Peng, Z.; Pelella, A.; Dun, C.; Urban, J. J.; Di Bartolomeo, A.; Casiraghi, C. All 2D Material Printed Diodes and Circuits on Paper for Sustainable Electronics. *ACS Nano* **2025**, *19* (34), 30833−30843.

(27) Martínez-Jódar, A.; Villar-Rodil, S.; Munuera, J. M.; Castro-Muñiz, A.; Coleman, J. N.; Raymundo-Piñero, E.; Paredes, J. I. Two-Dimensional MoS2 Nanosheets Derived from Cathodic Exfoliation for Lithium Storage Applications. *Nanomaterials* **2024**, *14* (11), No. 932.

(28) Wang, S.; Xue, J.; Xu, D.; He, J.; Dai, Y.; Xia, T.; Huang, Y.; He, Q.; Duan, X.; Lin, Z. Electrochemical Molecular Intercalation and Exfoliation of Solution-Processable Two-Dimensional Crystals. *Nat. Protoc.* **2023**, *18* (9), 2814−2837.

(29) Karger, L.; Synnatschke, K.; Settele, S.; Hofstetter, Y. J.; Nowack, T.; Zaumseil, J.; Vaynzof, Y.; Backes, C. The Role of Additives in Suppressing the Degradation of Liquid-Exfoliated WS2Monolayers. *Adv. Mater.* **2021**, *33* (42), No. 2102883.

(30) Harvey, A.; Backes, C.; Boland, J. B.; He, X.; Griffin, A.; Szydlowska, B.; Gabbett, C.; Donegan, J. F.; Coleman, J. N. Non-Resonant Light Scattering in Dispersions of 2D Nanosheets. *Nat. Commun.* **2018**, *9* (1), No. 4553.

(31) Backes, C.; Smith, R. J.; McEvoy, N.; Berner, N. C.; McCloskey, D.; Nerl, H. C.; O'Neill, A.; King, P. J.; Higgins, T.; Hanlon, D.; Scheuschner, N.; Maultzsch, J.; Houben, L.; Duesberg, G. S.; Donegan, J. F.; Nicolosi, V.; Coleman, J. N. Edge and Confinement Effects Allow in Situ Measurement of Size and Thickness of Liquid-Exfoliated Nanosheets. *Nat. Commun.* **2014**, *5* (1), No. 4576.

(32) Kubetschek, N.; Backes, C.; Goldie, S. Algorithm for Reproducible Analysis of Semiconducting 2D Nanomaterials Based on UV−VIS Spectroscopy. *Adv. Mater. Interfaces* **2024**, *11* (34), No. 2400311.

(33) Tongay, S.; Zhou, J.; Ataca, C.; Lo, K.; Matthews, T. S.; Li, J.; Grossman, J. C.; Wu, J. Thermally Driven Crossover from Indirect toward Direct Bandgap in 2D Semiconductors: MoSe2 versus MoS2. *Nano Lett.* **2012**, *12* (11), 5576−5580.

(34) Backes, C.; Szydłowska, B. M.; Harvey, A.; Yuan, S.; Vega-Mayoral, V.; Davies, B. R.; Zhao, P.; Hanlon, D.; Santos, E. J. G.; Katsnelson, M. I.; Blau, W. J.; Gadermaier, C.; Coleman, J. N. Production of Highly Monolayer Enriched Dispersions of Liquid-Exfoliated Nanosheets by Liquid Cascade Centrifugation. *ACS Nano* **2016**, *10* (1), 1589−1601.

(35) Yao, Y.; Ao, K.; Lv, P.; Wei, Q. MoS2 Coexisting in 1T and 2H Phases Synthesized by Common Hydrothermal Method for Hydrogen Evolution Reaction. *Nanomaterials* **2019**, *9* (6), No. 844.

(36) Fan, X.; Xu, P.; Li, Y. C.; Zhou, D.; Sun, Y.; Nguyen, M. A. T.; Terrones, M.; Mallouk, T. E. Controlled Exfoliation of MoS2 Crystals into Trilayer Nanosheets. *J. Am. Chem. Soc.* **2016**, *138* (15), 5143−5149.

(37) Lee, C.; Yan, H.; Brus, L. E.; Heinz, T. F.; Hone, J.; Ryu, S. Anomalous Lattice Vibrations of Single- and Few-Layer MoS2. *ACS Nano* **2010**, *4* (5), 2695−2700.

(38) Kang, N.; Paudel, H. P.; Leuenberger, M. N.; Tetard, L.; Khondaker, S. I. Photoluminescence Quenching in Single-Layer MoS2 via Oxygen Plasma Treatment. *J. Phys. Chem. C* **2014**, *118* (36), 21258−21263.

(39) Lamba, N. K.; Choudhary, P.; Kaushik, J.; Tripathi, K. M.; Choudhary, S. K.; Sonkar, S. K. Deploying Used Solid Carbon Dioxide to Assist Graphite Exfoliation. *New J. Chem.* **2024**, *48* (18), 8030−8033.

(40) Li, H.; Zhang, Q.; Yap, C. C. R.; Tay, B. K.; Edwin, T. H. T.; Olivier, A.; Baillargeat, D. From Bulk to Monolayer MoS2: Evolution of Raman Scattering. *Adv. Funct. Mater.* **2012**, *22* (7), 1385−1390.

(41) Sonker, A. K.; Xiong, S.; Aggarwal, R.; Olsson, M.; Spule, A.; Hosseini, S.; Sonkar, S. K.; Matic, A.; Westman, G. Exfoliated MoS2 Nanosheet/Cellulose Nanocrystal Flexible Composite Films as Electrodes for Zinc Batteries. *ACS Appl. Nano Mater.* **2023**, *6* (10), 8270−8278.

(42) Gosch, J.; Synnatschke, K.; Stock, N.; Backes, C. Comparative Study of Sonication-Assisted Liquid Phase Exfoliation of Six Layered Coordination Polymers. *Chem. Commun.* **2022**, *59* (1), 55−58.

(43) Dickinson, R. G.; Pauling, L. The Crystal Structure of Molybdenite. *J. Am. Chem. Soc.* **1923**, *45* (6), 1466−1471.

(44) Lotya, M.; Hernandez, Y.; King, P. J.; Smith, R. J.; Nicolosi, V.; Karlsson, L. S.; Blighe, F. M.; De, S.; Wang, Z.; McGovern, I. T.; Duesberg, G. S.; Coleman, J. N. Liquid Phase Production of Graphene by Exfoliation of Graphite in Surfactant/Water Solutions. *J. Am. Chem. Soc.* **2009**, *131* (10), 3611−3620.

(45) Israelachvili, J. N. *Intermolecular and Surface Forces*, 3rdrd ed.; Academic Press: San Diego, 2011.

(46) Rubinstein, M.; Colby, R. H. *Polymer Physics*; OUP Oxford, 2003.

(47) Neilson, J.; Avery, M. P.; Derby, B. Tiled Monolayer Films of 2D Molybdenum Disulfide Nanoflakes Assembled at Liquid/Liquid Interfaces. *ACS Appl. Mater. Interfaces* **2020**, *12* (22), 25125−25134.

(48) Cassidy, O.; Synnatschke, K.; Munuera, J. M.; Gabbett, C.; Carey, T.; Doolan, L.; Caffrey, E.; Coleman, J. N. Layer-by-Layer Assembly Yields Thin Graphene Films with near Theoretical Conductivity. *Npj 2D Mater. Appl.* **2025**, *9* (1), No. 2.

(49) Qiu, H.; Pan, L.; Yao, Z.; Li, J.; Shi, Y.; Wang, X. Electrical Characterization of Back-Gated Bi-Layer MoS2 Field-Effect Transistors and the Effect of Ambient on Their Performances. *Appl. Phys. Lett.* **2012**, *100* (12), No. 123104.

(50) Cunningham, G.; Khan, U.; Backes, C.; Hanlon, D.; McCloskey, D.; Donegan, J. F.; Coleman, J. N. Photoconductivity of Solution-Processed MoS2 Films. *J. Mater. Chem. C* **2013**, *1* (41), 6899−6904.

(51) Mukherjee, S.; Wang, S.; Venkatakrishnarao, D.; Tarn, Y.; Talha-Dean, T.; Lee, R.; Verzhbitskiy, I. A.; Huang, D.; Mishra, A.; John, J. W.; Das, S.; Bussolotti, F.; Maddumapatabandi, T. D.; Teh, Y. W.; Ang, Y. S.; Goh, K. E. J.; Lau, C. S. Toward Phonon-Limited Transport in Two-Dimensional Transition Metal Dichalcogenides by Oxygen-Free Fabrication. *ACS Nano* **2025**, *19* (9), 9327−9339.

(52) Cheng, Z.; Pang, C.-S.; Wang, P.; Le, S. T.; Wu, Y.; Shahrjerdi, D.; Radu, I.; Lemme, M. C.; Peng, L.-M.; Duan, X.; Chen, Z.; Appenzeller, J.; Koester, S. J.; Pop, E.; Franklin, A. D.; Richter, C. A. How to Report and Benchmark Emerging Field-Effect Transistors. *Nat. Electron.* **2022**, *5* (7), 416−423.

(53) Coleman, E.; Kelly, A.; Gabbett, C.; Doolan, L.; Liu, S.; Yadav, N.; Vij, J. K.; Coleman, J. N. Extracting the Temperature Dependence of Both Nanowire Resistivity and Junction Resistance from Electrical Measurements on Printed Silver Nanowire Networks. *ACS Appl. Electron. Mater.* **2025**, *7* (2), 806−815.

(54) Caffrey, E.; Carey, T.; Doolan, L.; Dawson, A.; Coleman, E.; Sofer, Z.; Cassidy, O.; Gabbett, C.; Coleman, J. N. Using Electrical Impedance Spectroscopy to Separately Quantify the Effect of Strain on Nanosheet and Junction Resistance in Printed Nanosheet Networks. *Small* **2025**, *21* (5), No. 2406864.

(55) Nowack, T.; Bastonero, L.; Knickrehm, T.; Carey, T.; Cassidy, O.; Coleman, J. N.; Sofer, Z.; Synnatschke, K. R.; Marzari, N.; Backes,

https://doi.org/10.1021/acsami.5c24890
ACS Appl. Mater. Interfaces XXXX, XXX, XXX−XXX

C. Assessing Quality and Purity of MoS2 Nanosheets by Diffuse Reflectance IR Spectroscopy. *2D Mater.* **2025**, *12* (4), No. 045021.